Research Article | Vol. 30, No. 13 / 20 Jun 2022 / Optics Express 22410
Optics EXPRESS

Theoretical investigation on the elimination of the period chirp by deliberate substrate deformations

FLORIAN BIENERT,* THOMAS GRAF, AND MARWAN ABDOU AHMED

Universität Stuttgart, Institut für Strahlwerkzeuge (IFSW), Pfaffenwaldring 43, 70569 Stuttgart, Germany
florian.bienert@ifsw.uni-stuttgart.de

Abstract: We present a theoretical investigation on the approach of deliberately bending the substrate during the exposure within laser interference lithography to compensate for the period chirp. It is shown that the yet undiscovered function of the surface geometry, necessary to achieve the zero-chirp case (i.e. having a perfectly constant period over the whole substrate) is determined by a first-order differential equation. As the direct analytical solution of this differential equation is difficult, a numerical approach is developed, based on the optimization of pre-defined functions towards the unknown analytical solution of the differential equation by means of a Nelder-Mead simplex algorithm. By applying this method to a concrete example, we show that an off-center placement of the substrate with respect to the point sources is advantageous both in terms of achievable period and substrate curvature and that a fourth-order polynomial can greatly satisfy the differential equation leading to a root-mean-square deviation of only 1.4 pm with respect to the targeted period of 610 nm.

1. Introduction

Ever since the invention of chirped pulse amplification (CPA) in 1985 [1], systems enabling the temporal stretching and compression of laser pulses have been on the rise [2]. This applies equally for diffraction gratings, as they are the key components in many of these systems. They are especially advantageous to produce large dispersion, which is required for both stretching [3] and compressing [4] of high-power and high-energy pulses [5–7]. Besides their major role in CPA, diffraction gratings are also used for various other purposes in laser technology such as intra-cavity selection and stabilization of polarization and/or wavelength [8,9]. To create the gratings with periods in the range of 300 nm to 900 nm, techniques of the micro- and nano-industry are mostly used [6]. For lithography, which is the production step that defines the grating lines, various techniques are widely established today, such as electron beam (E-beam) writing, nanoimprint, and laser interference lithography (LIL). E-beam lithography offers high flexibility in terms of achievable structure geometries and single-digit nm resolution. However, it suffers from a comparatively slow writing speed, requires demanding operation in vacuum and the quality of the produced structures is affected by heating, stitching and proximity effects [10–17]. Nanoimprint is both much faster and cheaper than E-beam lithography. It however puts high requirements on the controlling of temperature, pressure and the displacement of the mechanical imprinting process and the produceable structures are limited to a specific period given by the master template, which in turn can be affected by resist contamination [10,18–22]. Theoretically, LIL is ideally suited for the generation of linear gratings. It has the potential to be fast and flexible at the same time [23,24] as it allows for the exposure of the resist in a single shot and an easy adaption of the period of the generated interference pattern. The so-called period chirp however is a persistent problem of this technique [25–29]. It results from the invalidity of the plane-wave approximation used for the exposure. The consequences are a spatially inhomogeneous period as

#458636 https://doi.org/10.1364/OE.458636
Journal © 2022 Received 16 Mar 2022; revised 21 Apr 2022; accepted 2 May 2022; published 6 Jun 2022

Optics EXPRESS

well as an inclination of the grating lines [30,31]. In a more recent technique, called scanning beam interference lithography (SBIL), only a small section of the interference pattern is used in order to significantly mitigate this problem [25,32]. While the period chirp is eliminated, SBIL however misses a lot of the advantages of classical LIL and adds higher complexity to the setup. Due to the scanning, the exposure becomes much more time-consuming and high-precision stages are required to ensure the movement of the substrate with an accuracy of a few nm in order to obtain the correct spacing between the grating lines (i.e. avoiding stitching defects) [33]. To avoid all these efforts and use the advantages of classical LIL while minimizing the problem of the period chirp, we pick up the idea of deliberately bending the substrate during exposure [34] to compensate for the curvature of the wave fronts. After the exposure, when the substrate retrieves its initial flat surface, the period is expected to be constant over the whole substrates' surface, i.e. with "zero" period chirp. As shown in the publication by Walsh and Smith [34], the substrates' surface function for which a constant period can be achieved is not easy and straightforward to determine. Although they found a mathematical approach to start with, the authors could not derive the required equations to address this challenge. They, therefore, simplified the problem of finding a solution for the surface's shape by neglecting the inclination of the interference fringes. By this, an improvement was observed but the problem was not fully solved. Our aim therefore was to find this yet unknown solution. We derive the equations required to calculate the surface geometry which allows for the full elimination of the period chirp in dependence of both the exposure parameters i.e., the geometrical arrangement and the illumination wavelength, as well as the grating period itself. After proving that the surface geometry is obtained by the solution of a first-order differential equation, a numerical approach is presented to determine its solution by transforming it into an optimization problem. The application of this numerical approach is discussed on the basis of a concrete example. Furthermore, we prove the correctness of this numerical approach and the found solution by checking the results obtained for the considered example with the mathematical model presented in our latest contribution [31]. Finally, it is shown that the derived equations can also serve to intentionally create targeted chirps, e.g., a linearly increasing grating period.

2. Modeling

The common LIL setups employ a fiber-coupled laser whose beam is first split and subsequently superimposed on the substrate in order to generate a two-beam interference pattern. This can be implemented using a beam splitter or by means of a mirror which is oriented perpendicular to the substrate in the so-called Lloyd-configuration [23,24], as shown in Fig. 1(a) and (b), respectively.

For the setup comprising the beam splitter, the beam exiting the fiber is collimated at first. Subsequently, the beam is split into two replicas which are then focused through apertures in order to create the required divergence and to clean up the beam. The beam is then divergently guided towards the substrate interfering under an angle θ (at the center). Due to the exposure of the substrate to the beams' far-field, the setup can be validly modeled using the interference of the spherical waves emitted from two point sources [31]. The two point sources are thereby located at the foci, having a distance d to the substrate's center and are indicated with A and B in Fig. 1. One consequence of the chirp, the locally varying period on the surface of the substrate, is represented by the yellow curve in Fig. 1(a). The period increases approximately quadratically with increasing distance from the substrate's center, both in the x- (shown in the graph) and in the y-direction (perpendicular to the drawing plane).

The second setup, which uses a Lloyds-mirror to create a virtual second point source is much simpler, but the resulting chirp is different from the one of the first setup, as seen from the comparison between Fig. 1(a) and (b). Owing to the Lloyds-mirror which is intrinsically positioned exactly between the two point sources, a unidirectional chirp (yellow curve) is created, rising from the left to the right side of the exposed area on the substrate.

Optics EXPRESS

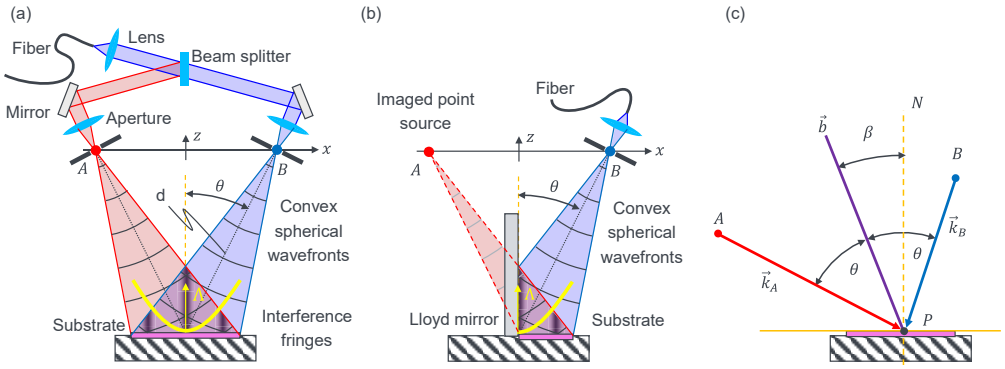

Fig. 1. (a): LIL setup using a beam splitter to create the two-beam inference pattern on the substrate. The exposure can mathematically be modelled as the interference of the spherical waves of two point sources. (b): LIL setup using a so-called Lloyds-mirror to create a virtual second point source. A one-sided chirp is created. (c): Mathematical abstraction of the setups shown in (a) and (b).

As we have recently shown in our latest publication, based on the model of the interference of the spherical waves of two point sources, three different exposure cases are possible, each being the abstraction of a different setup [31]. Within the present work we solely focus on the case shown in Fig. 1 (i.e., interference of the waves of two point sources with convex spherical wavefronts) for the following reasons. First, the setups underlying this case are widely used in practice as they do not require large optical components, thus making it very cost-effective. Secondly, it also corresponds to the model on which the publication of Walsh and Smith was based. And third, it creates a smaller chirp than the interference between convex and concave wave-fronts [31].

3. Deriving the function for the "zero" period-chirp geometry

The required deformation (shape) of the substrate during the exposure in order to obtain a constant period after it retrieves its initial flat surface is derived in the following. For this purpose, we first recall the calculation of the period obtained in a two-dimensional cartesian system. Such a system is shown in Fig. 1(c), being the mathematical abstraction of the setups shown in Fig. 1(a) and (b). The period Λ resulting from the interference of the spherical wavefronts originating from the two point sources A and B is determined at a point P on the substrate S. By considering an infinitely small region around the point P, the interference can be assumed to occur between two plane waves having the directional-vectors $\overrightarrow{k}_A$ and $\overrightarrow{k}_B$. The period of the resulting interference pattern is then given by

$$\Lambda(\beta, \theta, \lambda) = \frac{\lambda}{2 \cdot \sin(\theta) \cdot \cos(\beta)}, \tag{1}$$

where λ is the wavelength of the interfering beams, θ the angle between the directional-vectors, $\overrightarrow{b}$ their bisector, and β the angle between the bisector $\overrightarrow{b}$ to the normal of the substrate N. This equation was shown in a similar way by Kim et. al [29]. The task now is to transfer this two-dimensional consideration to a three-dimensional arrangement with a deformed substrate. The coordinate system shown in Fig. 2(a) is used for this purpose. The point sources A and B are arranged on the x-axis at $(-x_{PS}, 0, 0)$ and $(x_{PS}, 0, 0)$, respectively. The substrate's surface S defined by $z_S(x, y)$ is positioned below the two point sources. This function $z_S(x, y)$ must be found so that the interference of the spherical wavefronts emitted by the two point sources A and B exhibits a constant period Λ_{aim} across the whole substrate. In order to find this function, it is

Optics EXPRESS

beneficial to exploit the rotational symmetry of the interference between the spherical waves emitted from the two point sources and thus reduce the problem into two parts. To this end we first determine the curve C (shown in magenta) which lies in the xz-plane including the two point sources and on which the chirp is zero. This curve is then rotated around the x-axis which connects the two point sources, as indicated by the white arrow, to obtain the surface S. The period of the interference pattern on the entire surface S is then equal to the one along the curve C.

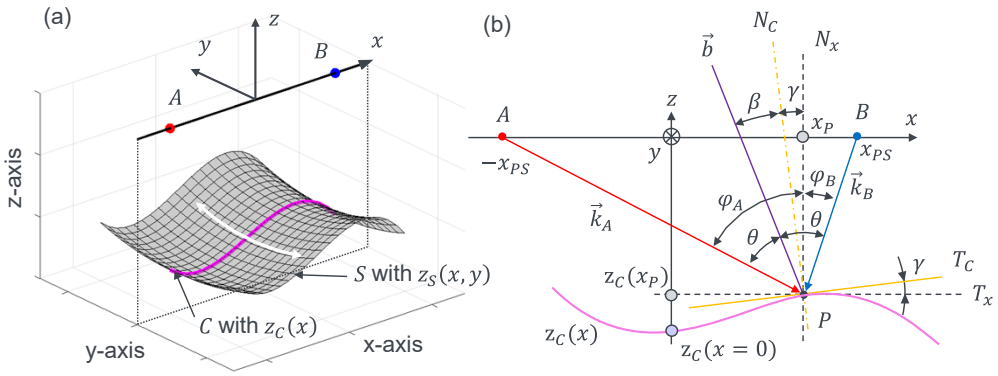

Fig. 2. Model for the determination of the surface function S to achieve a period with zero chirp. (a): Three-dimensional view on the model showing the point sources A and B and an exemplary surface function S created from the rotation of the exemplary curve C around the x-axis. (b): Two-dimensional view of the model shown in (a). The required angles and axes for the derivations are shown.

For the determination of the curve C defined by $z_C(x)$, we extend the arrangement presented in Fig. 1(c) to the one shown in Fig. 2(b), where the period at an arbitrary point P on the curve C is to be determined. In contrast to the arrangement in Fig. 1(c) the underlying curve is not straight so additional parameters have to be introduced.

The position of the point $P = (x_P, y_P, z_P)$ on the curve C is given by $(x_P, 0, z_C(x_P))$. The solid orange line T_C in Fig. 2(b) corresponds to the tangent of the curve C at the point P and therefore represents the local orientation of the curve C. This tangent is tilted by an angle γ with respect to the horizontal line T_x, which also passes through the point P but is oriented parallel to the x-axis. This angle γ also appears between the normal N_C of the curve C and the normal N_x of the x-axis in the xz-plane.

As shown in Eq. (1), the period can be calculated using the angle θ and the angle β between the bisector $\vec{b}$ and the surface normal N, represented by the dashed orange line in Fig. 1(c). Using the geometrical relationships shown in Fig. 2(b), β and θ can be expressed by

$$\beta = \frac{\varphi_A - \varphi_B}{2} - \gamma \tag{2}$$

and

$$\theta = \frac{\varphi_A + \varphi_B}{2} \tag{3}$$

using the angle φ_A between N_x and $\vec{k}_A$ and the angle φ_B between N_x and $\vec{k}_B$. The angles φ_A and φ_B in turn are defined by

$$\varphi_A(x_P, x_{PS}, z_C(x_P)) = \arctan\left(\frac{x_{PS} + x_P}{-z_C(x_P)}\right) \tag{4}$$

Optics EXPRESS

and

$$\varphi_B(x_P, x_{PS}, z_C(x_P)) = \arctan\left(\frac{x_{PS} - x_P}{-z_C(x_P)}\right). \tag{5}$$

Inserting Eqs. (2) and (3) into Eq. (1), the period Λ can be defined as

$$\Lambda(\gamma, \lambda, \varphi_A, \varphi_B)|_{x=x_P} = \frac{\lambda}{2 \cdot \sin\left(\frac{\varphi_A+\varphi_B}{2}\right) \cdot \cos\left(\frac{\varphi_A-\varphi_B}{2} - \gamma\right)}. \tag{6}$$

The angle γ is defined by the first derivative of the curve C, hence

$$\tan(\gamma) = \frac{dz_C(x_P)}{dx}. \tag{7}$$

Inserting Eq. (6) into Eq. (7) one obtains the differential equation

$$\frac{dz_C(x_P)}{dx} = \tan\left(\frac{\varphi_A - \varphi_B}{2} - \arccos\left(\frac{\lambda}{2 \cdot \sin\left(\frac{\varphi_A+\varphi_B}{2}\right) \cdot \Lambda}\right)\right). \tag{8}$$

With the Eqs. (4) and (5) this reads

$$\begin{aligned}\frac{dz_C(x)}{dx} = \tan\Bigg(&\frac{1}{2} \cdot \arctan\left(\frac{x_{PS} + x}{-z_C(x)}\right) - \frac{1}{2} \cdot \arctan\left(\frac{x_{PS} - x}{-z_C(x)}\right) \\ &- \arccos\left(\lambda \cdot \left(2 \cdot \sin\left(\frac{1}{2} \cdot \arctan\left(\frac{x_{PS} + x}{-z_C(x)}\right) + \frac{1}{2} \cdot \arctan\left(\frac{x_{PS} - x}{-z_C(x)}\right)\right) \cdot \Lambda\right)^{-1}\right)\Bigg)\end{aligned} \tag{9}$$

The solution of this differential equation yields the required curve C defined by $z_C(x)$ on which the period is Λ. It is worth pointing out that, although the derivation was made with the goal to achieve a constant period along the curve C, Eq. (9) can also be used to calculate the curve C needed to obtain a given spatial variation of the period by simply replacing Λ by $\Lambda(x)$. Once the curve C has been calculated, it just needs to be rotated around the x-axis to form the surface S with the desired period $\Lambda = \text{const.}$ or $\Lambda(x)$. Since the solution of the differential equation however proved to be very demanding, even by means of numerical methods, a method to obtain the solution with the help of an optimizer is presented in the following.

4. Numerical solution for the "zero" period-chirp geometry

A numerical optimizer-based method is introduced in this section to approximate the solution of the differential Eq. (9). It is developed on the basis of a concrete example with the aim to reach a constant period of Λ_{aim}= 610 nm on a substrate with a dimension of 100 mm x 100 mm. The illumination is chosen to occur with a wavelength of $\lambda = 415$ nm. Using Eq. (1) with $\beta = 0°$, this yields an angle of incidence of $\theta = 19.89°$ at the center of the substrate. The distance d (see Fig. 1(a)) is chosen to be 1000 mm, yielding a positioning of the point sources at x_{PS}= 340.2 mm and the center of the substrate at $z_C(x = 0)$= −940.4 mm (in the case of a flat substrate). To find an analytical expression for the curve C, the approach is to optimize the coefficients of a specific pre-defined function in such a way that the period chirp is eliminated as well as possible. A second-order polynomial (referred to with the index 2p in the following), a fourth-order polynomial (index 4p), a hyperbola (index h), an ellipse (index e), a spherical function (index s), and a sum-function (index h4p) consisting of a hyperbola and a fourth-order polynomial are investigated for this purpose. In case of the fourth-order polynomial the optimization function

Optics EXPRESS

$z_{C,opt}(x)$ reads

$$z_{C,opt,4p}(x) = a_4 \cdot x^4 + a_3 \cdot x^3 + a_2 \cdot x^2 + a_1 \cdot x^1 + a_0 \tag{10}$$

and the derivative yields

$$z'_{C,opt,4p}(x) = \frac{dz_{C,opt,4p}(x)}{dx} = 4a_4 \cdot x^3 + 3a_3 \cdot x^2 + 2a_2 \cdot x^1 + a_1 \tag{11}$$

Suitable starting values of the coefficients used in the definition of the optimization functions $z_{C,opt}(x)$ are chosen in a first step. In order to define a good starting point to achieve a fast convergence for the optimizer, the coefficients of all functions are chosen such that a flat substrate is formed that leads to the target period in the center. For the fourth-order polynomial (index 4p) the coefficients a_1 to a_4 are thus set to zero while a_0 is set to −940.4 mm. Subsequently the optimization function $z_{C,opt}(x)$ and it's derivative $z'_{C,opt}(x)$ are inserted into the equations (4) to (7) to determine the period function $\Lambda_{opt}(x)$ resulting along the curve $C_{opt} = (x, 0, z_{C,opt}(x))$. To quantify the deviation between the period functions $\Lambda_{opt}(x)$ and $\Lambda_{aim}(x) = \Lambda_{aim} = 610$ nm we define

$$D(a_4, \ldots, a_0) = \int_{Substrate} (\Lambda_{aim}(x) - \Lambda_{opt}(x))^2 dx \tag{12}$$

Minimizing this deviation D with a Nelder-Mead simplex algorithm [35,36] yields the coefficients of the optimization functions $z_{C,opt}(x)$.

The functions resulting from this optimization are shown in Fig. 3. Their shapes and their derivatives are shown in Fig. 3(a) by the solid and dashed lines, respectively. The resulting periods are shown in Fig. 3(b). The results for the plane substrate (index 0p) are shown in black as a reference. It is noticeable that all geometries lead to a lower chirp than the one obtained with a plane substrate. The optimization of the spherically and the elliptically shaped substrates led to very similar geometries which are indistinguishable in the figure.

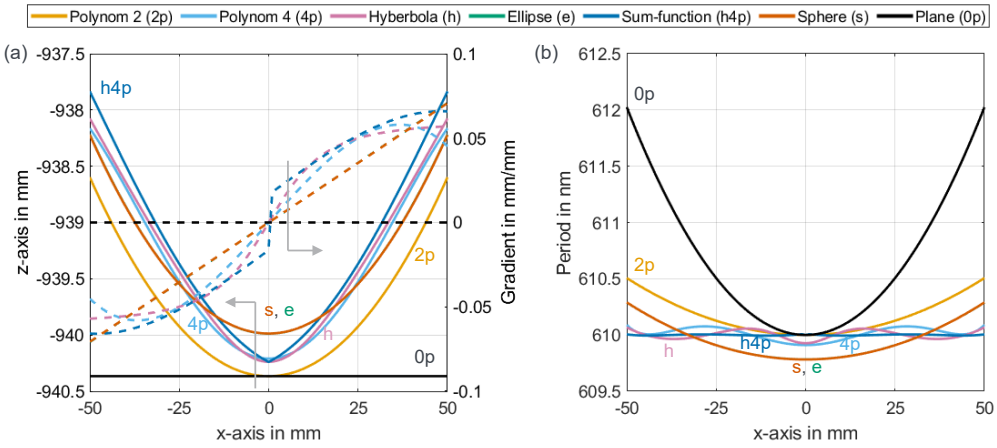

Fig. 3. Results of the optimization to find a curve C that leads to a constant period, i.e. a zero chirp for a concrete exposure example (see text). Different functions were tested to fit the solution of the differential equation Eq. (9). (a): Shapes and derivatives of the optimized functions represented by solid and dashed lines, respectively. (b): Resulting periods obtained with the corresponding curves shown in (a).

The best results are clearly obtained by the sum function (h4p) consisting of a hyperbola and a fourth-order polynomial, shown in red. However, while its period matches the targeted period, the required shape of the surface is problematic because the strong (but mathematically steady)

Optics EXPRESS

bending in the center is difficult to implement in practice and will most likely lead to a fracture of the substrate. If, however, the substrate would not be extended over the whole width, but only from $x = 0$ mm to 50 mm, the strong bending in the center could be avoided, while the period of 610 nm is still achieved. In practice this may be implemented by positioning the substrate off-center. Instead of finding a solution for the substrate's surface in the range of x = -50 mm to 50 mm, the solution is optimized within the boundaries from $x = 0$ mm to 100 mm. The results of this approach are shown in Fig. 4.

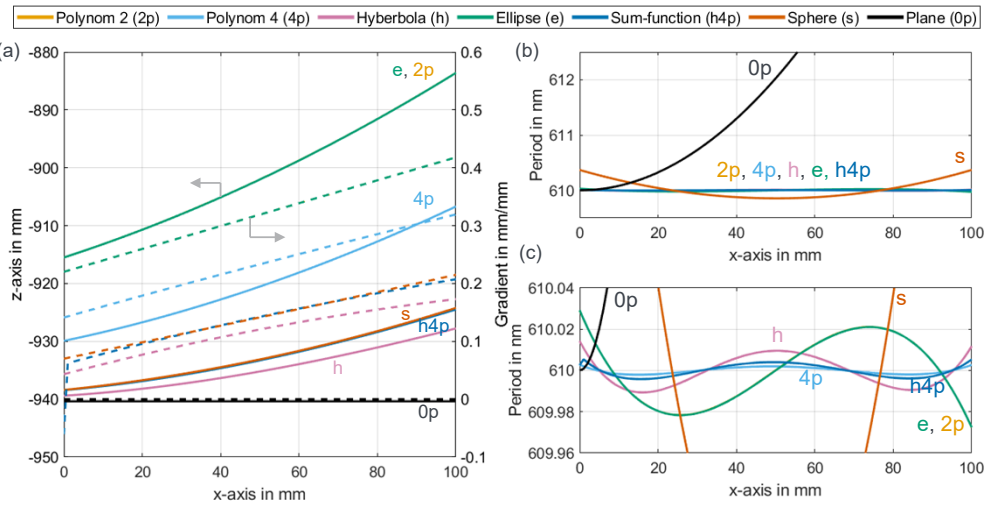

Fig. 4. Results of the optimization to find a curve C that has zero chirp for an off-center placement of the substrate. The same functions as for the previous case are investigated to fit the solution of the differential equation Eq. (9). (a): Shapes and derivatives of the optimized functions represented by the solid and the dashed lines, respectively. (b): Resulting periods obtained with the corresponding curves shown in (a). (c): Obtained periods with finer scaling.

The results obtained for the elliptically shaped substrate (index e) and the one described by the second-order polynomial (index 2p) cannot be distinguished in the chosen presentation. The comparison between the period distributions obtained in Fig. 3(b) to the ones from Fig. 4(b) shows significant improvements of the latter and that they are very close to the targeted constant period for all functions $z_{C,opt}(x)$ except for the spherically shaped (index s) substrate. In order to allow for a better comparison of the results, the period distributions are plotted again in Fig. 4(c) but with a higher scaling resolution. Especially the fourth-order polynomial (index 4p) shows good results, having only a remaining root-mean-square-Error (RMSE) of 1.4 pm and a maximum deviation of Δ_{max}= 2.7 pm. The good results also achieved with the other functions however equally underline the potential of the method to place the substrate off-center.

In order to obtain the zero-chirp surface S, the curve C needs to be rotated around the x-axis (see Fig. 2(a)). In Fig. 5 this is shown using the curve of the optimized fourth-order polynomial $C_{opt,4p}$ that was obtained in Fig. 4. In order to analyse, how well the goal of a constant period is achieved with this surface, the local period and the inclination of the interference lines were calculated along the surface $S_{opt,4p}$ using the equations derived in [31]. This was done to provide an independent proof of the correctness and functionality of the approaches presented in the present paper, i.e. the rotation of the curve C, the derived equations and the application of the optimizer.

The color-coded calculated period in Fig. 5(a) clearly shows the small deviation of the period $\Lambda_{opt}(x)$ obtained on the optimized surface based on the curve $C_{opt,4p}(x)$ from the target period

Optics EXPRESS

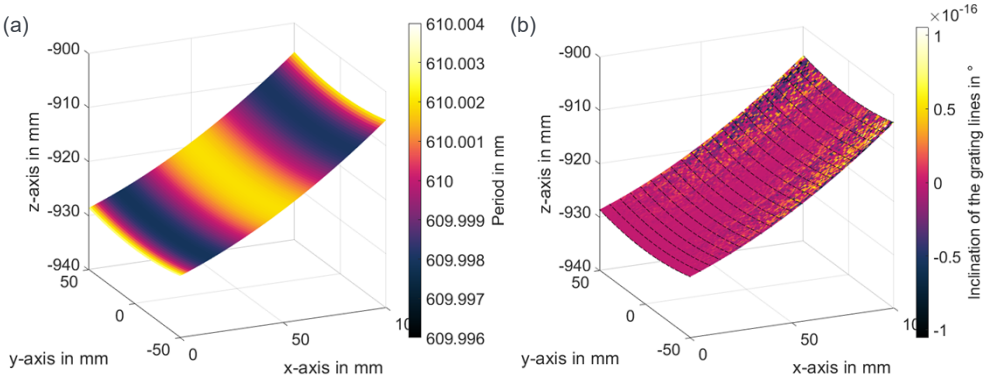

Fig. 5. Shape of the substrate optimized to obtain a constant period of the interference pattern (zero chirp) for the example described in the text. The surface is based on the rotation of the fourth-order polynomial shown in Fig. 4(a). Color-coded period $\Lambda_{opt}(x)$ (a) and inclination of the grating lines (represented by the black lines) and color-coded deviation from their ideal orientation (b) on this surface calculated using the equations from [31].

Λ_{aim}= 610 nm. The data also shows that, as expected, the period is constant along the rotational direction. Therefore, both the maximum deviation and the RMSE for the whole surface $S_{opt,4p}$ are identical to those of the curve $C_{opt,4p}$, i.e. $\Delta_{\max}$ = 2.7 pm and 1.4 pm. Figure 5(b) shows the investigation on the inclination of the grating lines. While the black lines indicate the orientation of the lines, the color-coded scale marks the deviation from their ideal orientation (i.e. their inclination). The results show that the grating lines are perfectly aligned which is also expected as this is an intrinsic consequence of the rotation of the curve C around the x-axis. The small deviations in the upper corners are attributed to numerical noise. In view of the negligible deviation between the obtained and the targeted period, the solution shown in Fig. 5 may be considered to be a "zero" period-chirp solution, since the remaining errors are much smaller than anything which is expected to be achievable in practice.

5. Discussion

When considering the off-center placement of the substrate it becomes obvious that it ideally suits the setup comprising the Lloyds-mirror (see Fig. 1(b)) where the substrate is intrinsically placed off-center. The use of the Lloyds-mirror is however typically accompanied by detrimental effects originating from flatness errors, scattering effects caused by the mirror's aperture and eventual dust particles, and problems in the uniformity of the linewidth [37,38]. For the present case, where a method is being specifically studied to achieve a constant period and perfectly straight grating lines, the setup shown in Fig. 1(a) might therefore be superior. An example on how our derived surface might be integrated into this setup is shown in Fig. 6(a). The substrate is fixed on an off-center positioned convexly shaped vacuum chuck (orange) which is tilted with respect to ground plate. While the overall tilt of the holder is used to realize the slope of the derived surface, its convex geometry creates the required curvature. For this implementation we see two main challenges. The first one is the creation of the required curvature, concerning both the holder and the substrate. For the holder we recommend a fabrication of a special vacuum chuck either by means of 3D-printing and appropriate post-processing or directly by milling, as this allows for the creation of the demanding geometry following a sphere in the one and a fourth-order-polynomial in the other direction. For the substrate, the pliability is of importance. For the derived geometry, the maximum deflection normal to the line connecting the substrate's edges is around 2.2 mm. While this bending might be reasonable when using thin silicon wafers, it is demanding for thick

Optics EXPRESS

glass substrates. Investigations on this were already carried out for thin glasses in [39,40]. The second challenge concerns the problems arising with the tilt of the substrate with respect to the planes of constructive interference [31]. This tilt might lead to problems in the exposure of the resist (e.g., skew reflection on the substrate's surface) and especially lead to a tilt of the grating lines with respect to the substrate's normal [41] (not to confuse with the inclination of the grating lines). With the presented geometry, the maximum tilt is 8.5° compared to a maximum tilt of 2.7° when using a flat substrate. While the further addressing of these two challenges is beyond the scope of this publication, it shall be mentioned that both of them can be significantly eased by an increase of the exposure distance d. For demonstrative reasons it was chosen to be very short (1 m) and an increase will lead to a less deflected "zero" period-chirp geometry after the optimization. When calculating the same example presented above but with a distance of $d = 2$ m, a maximum grating tilt of 4°, a RMSE of 0.6 pm from the ideal period and a maximum deflection of 0.92 mm between the substrate's edges were achieved. These values could be additionally improved by adapting the optimiser to also take into account these values in addition to the period.

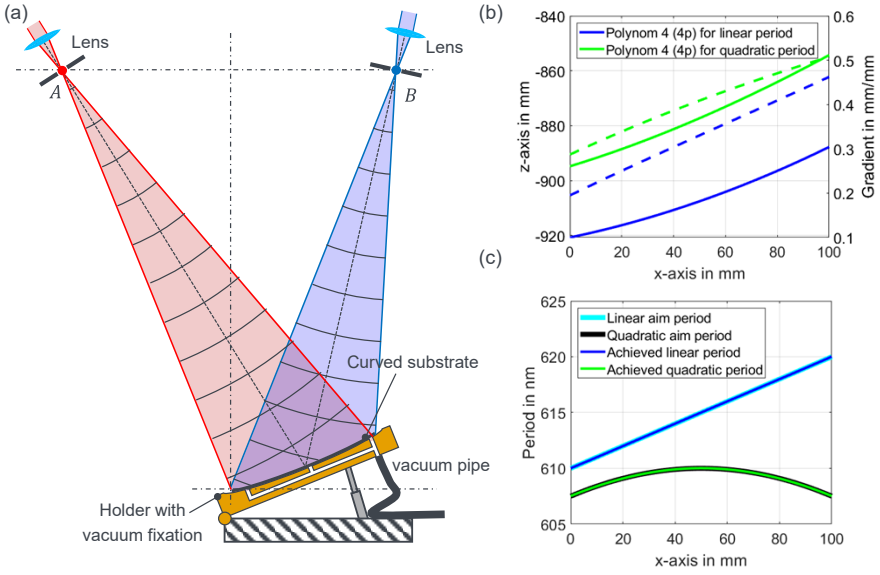

Fig. 6. (a): Exemplary setup used for the exposure of the curved substrate placed off-center. The deflection of the substrate is created by a vacuum chuck, while the slope is created by the tilt of the holder. (b): Curves and derivatives of the optimized functions to obtain deliberate chirps, represented by the solid and the dashed lines, respectively. (c): Targeted as well as achieved periods obtained by the corresponding curves shown in (b).

Due to the general definition of the equations derived in section 3, solutions can also be found for surface geometries aiming at non-constant period functions $\Lambda_{aim}(x)$; e.g. linearly increasing or quadratically decreasing periods might be beneficial for some applications. Results of the investigation on these two examples, utilizing again a fourth-order polynomial, are shown in Fig. 6(b) and (c). In Fig. 6(b) the optimized curves and their derivatives are depicted, while their targeted and obtained periods are shown in Fig. 6(c). The results clearly show a high agreement of the achieved period with the target period as well as a feasible surface geometry.

Optics EXPRESS

6. Summary and conclusion

Taking up the idea by Walsh and Smith [34], who proposed bending the substrate during exposure in order to eliminate the period chirp arising in LIL, we showed that the function describing the required surface geometry is given by the rotation of a curve C which itself is defined by a differential equation. Since the search for an analytical solution of this equation however proved to be very challenging, a numerical method was developed, showing that for a given example, a fourth-order polynomial placed off-center (with respect to the point sources) was able to satisfy the differential equation with an RMSE of 1.4 pm and a maximal deviation of less than 2.7 pm from the aim period of 610 nm. With respect to a flat substrate, which creates a maximum deviation of 2 nm, the chirp is reduced by almost three orders of magnitude. The remaining deviation is attributed to the deviation of the fourth-order polynomial from the ideal solution of the differential equation and could be reduced by using a higher-order polynomial and longer optimization times. A further investigation of this is however not considered to be reasonable, as the practical influences of both the exposure and the bending of the substrate itself are already likely to lead to errors that are larger than the presented deviations. Furthermore, we gave an example on how the substrate could be implemented in practice, including both the off-center placement and the creation of the required curvature.

Funding. European Commission (825246).

Acknowledgments. F. Bienert thanks Christoph Röcker for the valuable discussions and the support with the numerical solution of the problem.

Disclosures. The authors declare no conflicts of interest.

Data availability. No data were generated or analyzed in the presented research.

References

1. D. Strickland and G. Mourou, "Compression of amplified chirped optical pulses," Opt. Commun. **55**(6), 447–449 (1985).
2. I. V. Yakovlev, "Stretchers and compressors for ultra-high power laser systems," Quantum Electron. **44**(5), 393–414 (2014).
3. O. E. Martinez, "3000 times grating compressor with positive group velocity dispersion: Application to fiber compensation in 1.3-1.6 μm region," IEEE J. Quantum Electron. **23**(1), 59–64 (1987).
4. E. B. Treacy, "Optical Pulse Compression With Diffraction Gratings," IEEE J. Quantum Electron. **5**(9), 454–458 (1969).
5. C. Danson, D. Hillier, N. Hopps, and D. Neely, "Petawatt class lasers worldwide," High Power Laser Sci. Eng. **3**, e3–14 (2015).
6. N. Bonod and J. Neauport, "Diffraction gratings: from principles to applications in high-intensity lasers," Adv. Opt. Photonics **8**(1), 156 (2016).
7. S. Fu, W. Zhang, W. Kong, G. Wang, F. Xing, F. Zhang, and H. Zhang, "Review of pulse compression gratings for chirped pulse amplification system," Opt. Eng. **60**(2), 1–28 (2021).
8. T. Dietrich, S. Piehler, M. Rumpel, P. Villeval, D. Lupinski, M. Abdou Ahmed, and T. Graf, "Highly-efficient continuous-wave intra-cavity frequency-doubled Yb:LuAG thin-disk laser with 1 kW of output power," Opt. Express **25**(5), 4917–4925 (2017).
9. M. M. Vogel, M. Rumpel, B. Weichelt, A. Voss, M. Haefner, C. Pruss, W. Osten, M. A. Ahmed, and T. Graf, "Single-layer resonant-waveguide grating for polarization and wavelength selection in Yb:YAG thin-disk lasers," Opt. Express **20**(4), 4024–4031 (2012).
10. X. Dai and H. Xie, "New methods of fabricating gratings for deformation measurements: A review," Opt. Lasers Eng. **92**, 48–56 (2017).
11. T. R. Groves, D. Pickard, B. Rafferty, N. Crosland, D. Adam, and G. Schubert, "Maskless electron beam lithography: Prospects, progress, and challenges," Microelectron. Eng. **61-62**, 285–293 (2002).
12. Y. Chen, "Nanofabrication by electron beam lithography and its applications: A review," Microelectron. Eng. **135**, 57–72 (2015).
13. U. D. Zeitner, M. Oliva, F. Fuchs, D. Michaelis, T. Benkenstein, T. Harzendorf, and E. B. Kley, "High performance diffraction gratings made by e-beam lithography," Appl. Phys. A: Mater. Sci. Process. **109**(4), 789–796 (2012).
14. Y. Chang, R. Liu, and S. Fang, "EUV and E-Beam Manufacturability : Challenges and Solutions Categories and Subject Descriptors," 1–6 (2015).

Optics EXPRESS

15. A. C. Wei, W. A. Beckman, R. L. Engelstad, J. W. Mitchell, T. N. Phung, and J.-F. Zheng, "Localized resist heating due to electron-beam patterning during photomask fabrication," *20th Annu. BACUS Symp. Photomask Technol.* 4186, 482–493 (2001).
16. A. You, M. A. Y. Be, and I. In, "Proximity effect in electron-beam lithography," J. Vac. Sci. Technol. (N. Y., NY, U. S.) **12**(6), 1271–1275 (1975).
17. R. K. Dey and B. Cui, "Stitching error reduction in electron beam lithography with in-situ feedback using self-developing resist," J. Vac. Sci. Technol., B: Nanotechnol. Microelectron.: Mater., Process., Meas., Phenom. **31**(6), 06F409 (2013).
18. L. J. Guo, "Recent progress in nanoimprint technology and its applications," J. Phys. D: Appl. Phys. **37**(11), R123–R141 (2004).
19. D. L. Voronov, E. M. Gullikson, and H. A. Padmore, "Large area nanoimprint enables ultra-precise x-ray diffraction gratings," Opt. Express **25**(19), 23334–23342 (2017).
20. H. Schift, "Nanoimprint lithography: An old story in modern times? A review," J. Vac. Sci. Technol., B: Microelectron. Nanometer Struct.–Process., Meas., Phenom. **26**(2), 458–480 (2008).
21. W. Zhang and S. Y. Chou, "Multilevel nanoimprint lithography with submicron alignment over 4 in. Si wafers," Appl. Phys. Lett. **79**(6), 845–847 (2001).
22. C. M. Sotomayor Torres, S. Zankovych, J. Seekamp, A. P. Kam, C. Clavijo Cedeno, T. Hoffmann, J. Ahopelto, F. Reuther, K. Pfeiffer, G. Bleidiessel, G. Gruetzner, M. V. Maximov, and B. Heidari, "Nanoimprint lithography: An alternative nanofabrication approach," Mater. Sci. Eng., C **23**(1-2), 23–31 (2003).
23. C. J. M. Van Rijn, "Laser interference as a lithographic nanopatterning tool," J. Microlithogr. Microfabr. Microsystems **5**(1), 011012 (2006).
24. C. Lu and R. H. Lipson, "Interference lithography: A powerful tool for fabricating periodic structures," Laser Photonics Rev. **4**(4), 568–580 (2010).
25. C. G. Chen, P. T. Konkola, R. K. Heilmann, G. S. Pati, and M. L. Schattenburg, "Image metrology and system controls for scanning beam interference lithography," J. Vac. Sci. Technol., B: Microelectron. Process. Phenom. **19**(6), 2335–2341 (2001).
26. A. Katzir, A. C. Livanos, J. B. Shellan, and A. Yariv, "Chirped Gratings in Integrated Optics," IEEE J. Quantum Electron. **13**(4), 296–304 (1977).
27. K. Hibino and Z. S. Hegedus, "Hyperbolic holographic gratings: analysis and interferometric tests," Appl. Opt. **33**(13), 2553–2559 (1994).
28. J. Ferrera, "Analysis of distortion in interferometric lithography," J. Vac. Sci. Technol., B: Microelectron. Process. Phenom. **14**(6), 4009–4013 (1996).
29. H. Kim, H. Jung, D.-H. Lee, K. B. Lee, and H. Jeon, "Period-chirped gratings fabricated by laser interference lithography with a concave Lloyd's mirror," Appl. Opt. **55**(2), 354–359 (2016).
30. S.-T. Zhou, Z.-Q. Lin, and W. S. C. Chang, "Precise periodicity control in the fabrication of holographic gratings," Appl. Opt. **20**(8), 1270–1272 (1981).
31. F. Bienert, T. Graf, M. Abdou Ahmed, and M. A. Ahmed, "Comprehensive theoretical analysis of the period chirp in laser interference lithography," Appl. Opt. **61**(9), 2313–2326 (2022).
32. C. G. Chen, P. T. Konkola, R. K. Heilmann, C. Joo, and M. L. Schattenburg, "Nanometer-accurate grating fabrication with scanning beam interference lithography," Nano- Microtechnology Mater. Process. Packag. Syst. **4936**, 126–134 (2002).
33. P. T. Konkola, C. G. Chen, R. K. Heilmann, C. Joo, J. C. Montoya, C.-H. Chang, and M. L. Schattenburg, "Nanometer-level repeatable metrology using the Nanoruler," J. Vac. Sci. Technol., B: Microelectron. Process. Phenom. **21**(6), 3097–3101 (2003).
34. M. E. Walsh and H. I. Smith, "Method for reducing hyperbolic phase in interference lithography," J. Vac. Sci. Technol., B: Microelectron. Process. Phenom. **19**(6), 2347–2352 (2001).
35. J. A. Nelder and R. Mead, "A Simplex Method for Function Minimization," Comput. J. **7**(4), 308–313 (1965).
36. J. C. Lagarias, J. A. Reeds, M. H. Wright, and P. E. Wright, "Convergence properties of the Nelder-Mead simplex method in low dimensions," SIAM J. Optim. **9**(1), 112–147 (1998).
37. Y.-J. Hung, H.-J. Chang, P.-C. Chang, J.-J. Lin, and T.-C. Kao, "Employing refractive beam shaping in a Lloyd's interference lithography system for uniform periodic nanostructure formation," J. Vac. Sci. Technol., B: Nanotechnol. Microelectron.: Mater., Process., Meas., Phenom. **35**(3), 030601 (2017).
38. T. B. O'Reilly and H. I. Smith, "Linewidth uniformity in Lloyd's mirror interference lithography systems," J. Vac. Sci. Technol., B: Microelectron. Nanometer Struct.–Process., Meas., Phenom. **26**(6), 2131–2134 (2008).
39. S. T. Gulati and J. D. Helfinstine, "Edge Strength Testing of Thin Glasses," Int. J. Appl. Glas. Sci. **2**(1), 39–46 (2011).
40. M. Y. Tsai, H. J. Chen, and J. H. Yeh, "Evaluation of bending strength of window glass substrate with considerations of uni- And bi-axial loading and free edge stresses," J. Electron. Packag. Trans. ASME **141**(4), 1–7 (2019).
41. M. E. Walsh, "On the design of lithographic interferometers and their application," 1–300 (2004).